

This manuscript has been submitted for publication to Geophysical Research Letters on 27th September 2022. If accepted, the final version of this manuscript will be available via the Peer-reviewed Publication DOI link printed on this webpage.

Title:

Linking earthquake magnitude-frequency statistics and stress in visco-frictional fault zone models

Authors:

Adam Beall^{1,2*}, twitter: @adambeallgeo

Martijn P.A. van den Ende^{3,4}, twitter: @martijnende

Jean-Paul Ampuero³, twitter: @DocTerremoto

Fabio A. Capitano², twitter: @fabiocapitano2

Åke Fagereng¹, twitter: @akefagereng

¹School of Earth and Environmental Sciences, Cardiff University, Cardiff, UK

²School of Earth, Atmosphere and Environment, Monash University, Victoria, Australia

³Université Côte d'Azur, IRD, CNRS, Observatoire de la Côte d'Azur, Géoazur, Valbonne, France

⁴Université Côte d'Azur, OCA, UMR Lagrange, France

Contact email:

adambeall1@gmail.com

1 **Linking earthquake magnitude-frequency statistics and stress in visco-**
2 **frictional fault zone models**

3 **Adam Beall^{1,2}, Martijn van den Ende³, Jean-Paul Ampuero³, Fabio A. Capitanio² and Åke**
4 **Fagereng¹**

5 ¹School of Earth and Environmental Sciences, Cardiff University, Cardiff, UK

6 ²School of Earth, Atmosphere and Environment, Monash University, Victoria, Australia

7 ³Université Côte d'Azur, IRD, CNRS, Observatoire de la Côte d'Azur, Géoazur, Valbonne,
8 France

9 Corresponding author: Adam Beall (adambeall1@gmail.com)

10 **Key Points:**

- 11 • Combining viscous creep and rate-and-state friction in fault slip models limits the peak
12 loading stress over the earthquake cycle.
- 13 • Numerical and analytical models reproduce Gutenberg-Richter earthquake size-
14 recurrence statistics, with a b-value linked to fault stress.
- 15 • The interplay between loading stress and probabilistic fault locking provides an
16 explanation for regional contrasts in b-value.
17

18 **Abstract**

19 The ability to estimate the likelihood of given earthquake magnitudes is critical for seismic
20 hazard assessment. Earthquake magnitude-recurrence statistics are empirically linked to stress,
21 yet which fault-zone processes explain this link remains debated. We use numerical models to
22 reproduce the interplay between viscous creep and frictional sliding of a fault-zone, for which
23 inter-seismic locking becomes linked to stress. The models reproduce the empirical stress-
24 dependent earthquake magnitude distribution observed in nature. Stress is related to the
25 likelihood a fault section is near frictional failure, influencing likely rupture lengths. An
26 analytical model is derived of a fault consisting of identical patches, each with a probability of
27 inter-seismic locking. It reproduces a similar magnitude-recurrence relationship, which may
28 therefore be caused by probabilistic clustering of locked fault patches. Contrasts in earthquake
29 statistics between regions could therefore be explained by stress variation, which has future
30 potential to further constrain statistical models of regional seismicity.

31 **Plain Language Summary**

32 The frequency of earthquakes with a given magnitude is empirically described by the Gutenberg-
33 Richter law, where large earthquakes occur less frequently than small ones. Variations in
34 magnitude distribution between regions have been correlated with the tectonic force acting on a
35 fault. However, it is unclear which mechanism is responsible for this relationship, restricting its
36 predictive capability. Here, we create computational models in which some portions of a fault
37 can generate earthquakes and others can move slowly (not generating earthquakes). This slow
38 movement acts to relax and limit the elastic forces that build up around the fault. This approach
39 is used to reproduce realistic earthquake statistics, indicating that processes that limit the stress
40 build-up between earthquakes may be responsible for the varying likelihoods of earthquake
41 magnitudes observed in nature.

42 **1 Introduction**

43 One of the cornerstones of modern seismic hazard assessment is the ability to model statistical
44 distributions of how often earthquakes of a given size occur in a region (Gerstenberger et al.,
45 2020). This is typically modelled following the Gutenberg-Richter (G-R) law, where the number
46 N of earthquakes of moment magnitude M_w or greater that occur in a specific region and time
47 period is given by $\log(N) = a - bM_w$. a and b are empirical parameters, which vary between
48 regions. For example, for thrust fault earthquakes, b is 0.75 at the Honshu subduction margin,
49 Japan, and 1.07 at the Marianas margin (Bilek & Lay, 2018). Higher b -values indicate that the
50 ratio of small to large earthquake rates is larger (large earthquakes are relatively less frequent).

51
52 A high b -value has been linked to low differential stress in laboratory experiments (Scholz,
53 1968). In nature, it has been correlated with extensional tectonic regimes (Schorlemmer et al.,
54 2005), shallow earthquake hypocenters (Spada et al., 2013), regions hosting inter-seismic creep
55 (Tormann et al., 2014) and periods following large earthquakes (Nuannin et al., 2005). These
56 contexts are generally associated with relatively low differential stress. The G-R distribution of
57 earthquake sizes is thought to reflect a power-law (fractal) distribution of material properties,
58 fault lengths or stress in the Earth, based on physical models
59 (Ampuero et al., 2006; Dublanchet, 2020; Huang & Turcotte, 1988; Kanamori & Anderson,
60 1975; King, 1983; Mogi, 1967; Scholz, 1968). An increase in the stress loading a material with a

61 power-law strength distribution results in a larger critically stressed fault area (Huang &
62 Turcotte, 1988; Scholz, 1968), while still reproducing the G-R law, leading to a predicted
63 decrease in b-value. However, this process is complicated by rupture dynamics over earthquake
64 cycles. Shear-stress evolves heterogeneously as fault segments slip, while also depending on
65 loading conditions. Earthquakes may also propagate through regions that are unfavorable for
66 earthquake nucleation, depending probabilistically on the magnitude and heterogeneity of fault
67 stress and strength (Ampuero et al., 2006; Fang & Dunham, 2013; Galis et al., 2015; Ripperger
68 et al., 2007). Earthquake cycle models can address these ambiguities by reproducing fault stress
69 states that evolve self-consistently and can be used to study the controls on rupture for various
70 fault structures, properties and conditions. Such models have been used to reproduce the G-R law
71 (Cattania, 2019; Dublanchet, 2020; Dublanchet et al., 2013; van den Ende et al., 2020), though
72 an outstanding question is how they can reproduce the observed b-value dependence on stress.

73
74 Faults commonly include ‘creeping’ regions where elastic strain does not accumulate (inter-
75 seismic coupling is low) and seismic slip is less likely (Avouac, 2015), influencing the
76 distribution of possible earthquake magnitudes. Creep may occur by stable frictional sliding or
77 viscous mechanisms. We use the term creep to refer exclusively to viscous deformation, which is
78 inferred from evidence of pressure solution creep (Gratier et al., 2013; Rutter, 1976) that
79 operates within fault-zones at depths typically including, but not limited to, 5-20 km (Bos &
80 Spiers, 2002). Fault segments with low inter-seismic coupling are inferred from b-values to
81 deform at low deviatoric stress (Tormann et al., 2014), which could be explained by viscous
82 stress relaxation. Building on these inferences, we hypothesize that the proportion of fault area
83 that is creeping is related to both fault stress and b-value, explaining why these are linked in
84 nature. We test this hypothesis by developing earthquake cycle models in which fault
85 deformation occurs by a combination of frictional sliding and viscous creep. Visco-frictional
86 fault-zones observed in nature are represented as a coupled fault and shear-zone, allowing us to
87 explore how stress relaxation due to shear-zone deformation (or off-fault creep) influences
88 earthquake size. Our modelled earthquake cycles involve a range of rupture dynamics that
89 depend on this visco-frictional interplay. The resulting catalogue of models reproduce the
90 relationship between stress and b-value. We also interpret these results through comparison to an
91 analytical model and demonstrate that it is the probability that a given fault segment is critically
92 stressed that controls the modelled earthquake statistics.

93
94

95 **2 Methodology**

96 **2.1 Numerical model**

97 We use the boundary element code QDYN (Luo et al., 2017) to model quasi-dynamic earthquake
98 cycles. QDYN solves the time- and position-dependent slip and slip-rate of a planar fault
99 embedded in two elastic half-spaces undergoing constant tectonic loading. Slip and slip-rate
100 depend on the elastic stress-state, while also relieving accumulated stress, providing a non-linear
101 relationship between stress and fault slip that may generate the spectrum of creep to seismic slip.
102 The coupled fault and shear-zone system is modelled on a 2-D vertical plane as a 1-D thrust
103 fault, neglecting along-strike variation, with a seismogenic zone of width $L_f = 30$ km. Along
104 unbounded extensions of the fault beyond its seismogenic zone, a steady slip velocity of $v_p = 10^{-}$

105 9 m s^{-1} is prescribed, representing plate motion of $\sim 30 \text{ mm/yr}$. On the seismogenic zone, a visco-
 106 frictional rheology is assumed in which total fault slip rate is the sum of viscous (v_v) and
 107 frictional (v_f) slip rates, such that the weakest mechanism dominates: at any given point on the
 108 fault we have (for bulk shear stress τ and frictional and viscous stresses τ_f and τ_v , respectively,
 109 and state variable θ):

$$\tau = \tau_f(v_f, \theta) = \tau_v(v_v) \quad (1)$$

110

$$v = v_f + v_v \quad (2)$$

111

112 Frictional strength is assumed to follow the rate-and-state law (equation S1), with frictional rate
 113 parameter $(a - b) = -0.011$, such that the fault would be velocity-weakening and potentially
 114 seismic in the absence of creep. The steady-state static and dynamic strengths S_f and S_d are
 115 defined as the frictional strengths prior to and during seismic sliding. They are $S_f = 60 \text{ MPa}$ and
 116 $S_d = 37 \text{ MPa}$, for the reference friction coefficient $\mu_0 = 0.6$, effective normal stress 100 MPa and
 117 calculated at steady slip rates of v_p and 1 m/s , respectively. We take S_f and S_d as constants for
 118 analysis, though they are an approximation as the models are not steady-state and ruptures may
 119 have partial stress drops. The earthquake nucleation length L_∞ (following Rubin & Ampuero,
 120 2005, Text S1), the size a slip zone must reach to become unstable, is 316 m for the chosen
 121 frictional parameters. L_b is the length-scale near a rupture front over which frictional weakening
 122 occurs and is approximately 150 m . A model resolution of 29.3 m is chosen to resolve both
 123 processes.

124

125 Viscous deformation is assumed to be Newtonian, following $\tau_v = v_v \eta / W$, for viscosity η and
 126 shear-zone width W . Fault-zones typically consist of mixtures of blocks of varying strengths and
 127 sizes that follow fractal distributions (Fagereng & Sibson, 2010; Kirkpatrick et al., 2021).
 128 Accordingly, the shear-zone consists of patches with random lengths from a truncated power-law
 129 distribution with exponent $D = 1$, ranging from 10 to 100 m . Each patch has a uniform η which
 130 is chosen by assuming that $\log(\eta)$ follows a uniform random distribution between $\eta_{min} = 10^{18}$
 131 Pa s and $\eta_{max} = 10^{20} \text{ Pa s}$. This reflects heterogeneity within the seismogenic zone inferred in
 132 nature (Fagereng & Sibson, 2010; Gratier et al., 2013) and microphysical models (Bos & Spiers,
 133 2002). W is uniform along the fault and constant for a given simulation. This setup could
 134 equivalently represent uniform η and down-dip W heterogeneity.

135

136 The model reproduces seismic and aseismic slip (Figure 1), with a range of rupture sizes,
 137 depending on visco-frictional interaction. For each simulation, an earthquake catalogue is
 138 compiled with moment magnitudes M_w computed by assuming that earthquake areas are
 139 circular.

140

141 As a consequence of the adopted rheology, there exists a critical viscosity η_c , where if a fault
 142 patch has $\eta > \eta_c$ it will be primarily inter-seismically locked and capable of accumulating elastic
 143 energy and possibly of nucleating earthquakes. The steady-state strength of the viscous material
 144 S_v is the stress at which it accommodates plate motion: $S_v = v_p \eta / W$. Inter-seismic elastic strain
 145 accumulation plateaus at a peak stress below the frictional steady-state strength S_f (i.e. tectonic
 146 deformation is fully accommodated by creep) if $S_v / S_f < 1$. The threshold $S_v / S_f = 1$
 147 corresponds to $\eta = \eta_c$, giving:

$$\eta_c = \frac{S_f W}{v_p} \quad (3)$$

148 ϕ is the probability that a given patch will be inter-seismically locked ($\eta > \eta_c$). A collection of
 149 adjacent locked patches is termed an ‘effective asperity’ (Figure 1a). ϕ is also approximately
 150 equivalent to the proportion of the fault consisting of effective asperities, converging to an exact
 151 agreement as the number of patches is increased. For the viscosity distribution of the reference
 152 model-set, the probability ϕ is:

$$\phi \equiv P(\eta \geq \eta_c) = \frac{\ln(\eta_{max}) - \ln(\eta_c)}{\ln(\eta_{max}) - \ln(\eta_{min})} \quad (4)$$

153
 154 ϕ is controlled by varying W (equation 3) and therefore η_c (equation 4). Variation of ϕ could be
 155 equivalently achieved by varying the normal stress or friction coefficient along the fault and
 156 therefore S_f , however this would also modify the earthquake nucleation length and stress drop,
 157 so we only vary W for simplicity. We could equally have changed v_p , but that would also affect
 158 the earthquake recurrence intervals. Note that the definitions of ϕ and η_c assume steady-state
 159 simulations. Our simulations are not steady-state and small proportions of viscous deformation
 160 can occur during inter-seismic periods, even for $\eta > \eta_c$. Inter-seismically creeping patches can
 161 experience some co- or post-seismic frictional sliding due to the elevated stresses of a
 162 propagating earthquake.

163
 164 We simulate regional scale variations in loading conditions by changing the key parameter ϕ , as
 165 average fault shear stress is shown to vary proportionally with ϕ up to a critical stress threshold
 166 (Figure 2a). ϕ is varied from 0.1 to 1 by varying W from 1000 m to 10 m. We run three models
 167 with different randomized realizations of the viscosity distribution for each ϕ , generating
 168 statistically significant earthquake catalogues for b-value analysis and testing the sensitivity to
 169 the randomized distribution.

170
 171 As fault shear stress varies spatially and temporally, we calculate the representative fault shear
 172 stress τ_{av} by calculating the spatially averaged shear stress for each time-step and then taking the
 173 temporal maximum (Figure S2). τ_{av} is typically the average stress prior to the largest
 174 earthquake. Model dynamics depend on the stress relative to fault strength, not on the absolute
 175 stress. Stress is non-dimensionalised as the ratio $\bar{\tau}_{av}$ between the average available static stress
 176 drop prior to the largest event (following the τ_{av} definition) and the strength drop (which is also
 177 the maximum possible stress drop):

$$\bar{\tau}_{av} = \frac{\tau_{av} - S_d}{S_f - S_d} \quad (4)$$

178 Further modelling methodology details are included in Text S1.

179

180 **2.2 Analytical asperity model**

181 We construct a simplified analytical model for comparison. In this model the fault consists of
 182 many permanent patches of identical length w , each with a constant probability ϕ of steady-state

183 inter-seismic locking and therefore of forming an effective asperity. The probability that a given
 184 effective asperity will consist of n patches is:

$$185 \quad P(n) = (1 - \phi)\phi^{n-1} \quad (5)$$

186
 187 To predict the statistics of ruptures, we assume that each effective asperity repeatedly hosts
 188 events rupturing that individual asperity only. We assume that a single patch can nucleate an
 189 earthquake, which is justified by the fact that L_∞ is only 1.2x the length of the smallest patch.
 190 We take the patch length $w = 550$ m, which is the average patch length in the QDYN models.
 191 From this simple probabilistic model, we calculate estimates of the b-value (derivation fully
 192 described in Text S3).
 193

194 **3 Results**

195 Models are run for 2,000 years, including a 500-year run-in period that is excluded from
 196 analysis. Earthquake stress drops are defined as the change in shear stress throughout an
 197 earthquake over the region it ruptured. Stress drops are relatively constant (standard deviation of
 198 4 MPa) with an average $\Delta\tau_{av} = 17$ MPa (74% of the maximum possible strength drop $S_f - S_d$
 199), within the range of seismological observations (Abercrombie, 1995). Events with $M_w > 5.5$
 200 tend to have lower stress drops (~ 7 MPa), because large ruptures can pass through low stress
 201 regions, as discussed by Lambert et al. (2021).
 202

203 The average stress τ_{av} increases linearly with increasing locking probability ϕ (Figure 2a),
 204 before plateauing at a peak value of approximately $S_f - \Delta\tau_{av}$. We define the value of ϕ where
 205 $\tau_{av} = S_f - \Delta\tau_{av}$ as ϕ_y . While $\tau_{av} < S_f$, fault segments locally reach S_f to nucleate earthquakes,
 206 which can propagate through regions with $\tau < S_f$. We also derive τ_{av} from the expected value of
 207 average viscosity (Text S3.1), giving equation 6, which depends on the choice of viscosity
 208 contrast $\Delta\eta = \eta_{max} - \eta_{min}$ and agrees with the numerical results.
 209

$$209 \quad \tau_{av} \approx \begin{cases} \phi S_f + \frac{(1 - \phi)S_f}{\Delta\eta^{0.5(1-\phi)}} & \phi < \phi_y \\ S_f - \Delta\tau_{av} & \phi > \phi_y \end{cases} \quad (6)$$

210
 211 The relationship between ϕ and τ_{av} is therefore clear, where high fault-scale shear stress reflects
 212 an increased likelihood of patch locking.
 213

214 At low ϕ and τ_{av} , earthquakes are generally limited to small isolated effective asperities (black
 215 stripes in Figure 1b). Earthquakes rarely propagate into adjacent creeping regions, and are
 216 restricted to low magnitudes ($M_w < 5.7$ and on average $M_w \sim 4$).
 217

218 With increasing ϕ and consequently higher τ_{av} , effective asperities of increasing sizes can host
 219 larger earthquakes (Figure 1c-d), that also occasionally span multiple asperities. Small
 220 earthquakes also persist, both hosted on small effective asperities and occurring as partial
 221 ruptures of larger effective asperities. When $\phi = 0.61$, $\tau_{av} = 47$ MPa ($\bar{\tau}_{av} = 0.43$) and

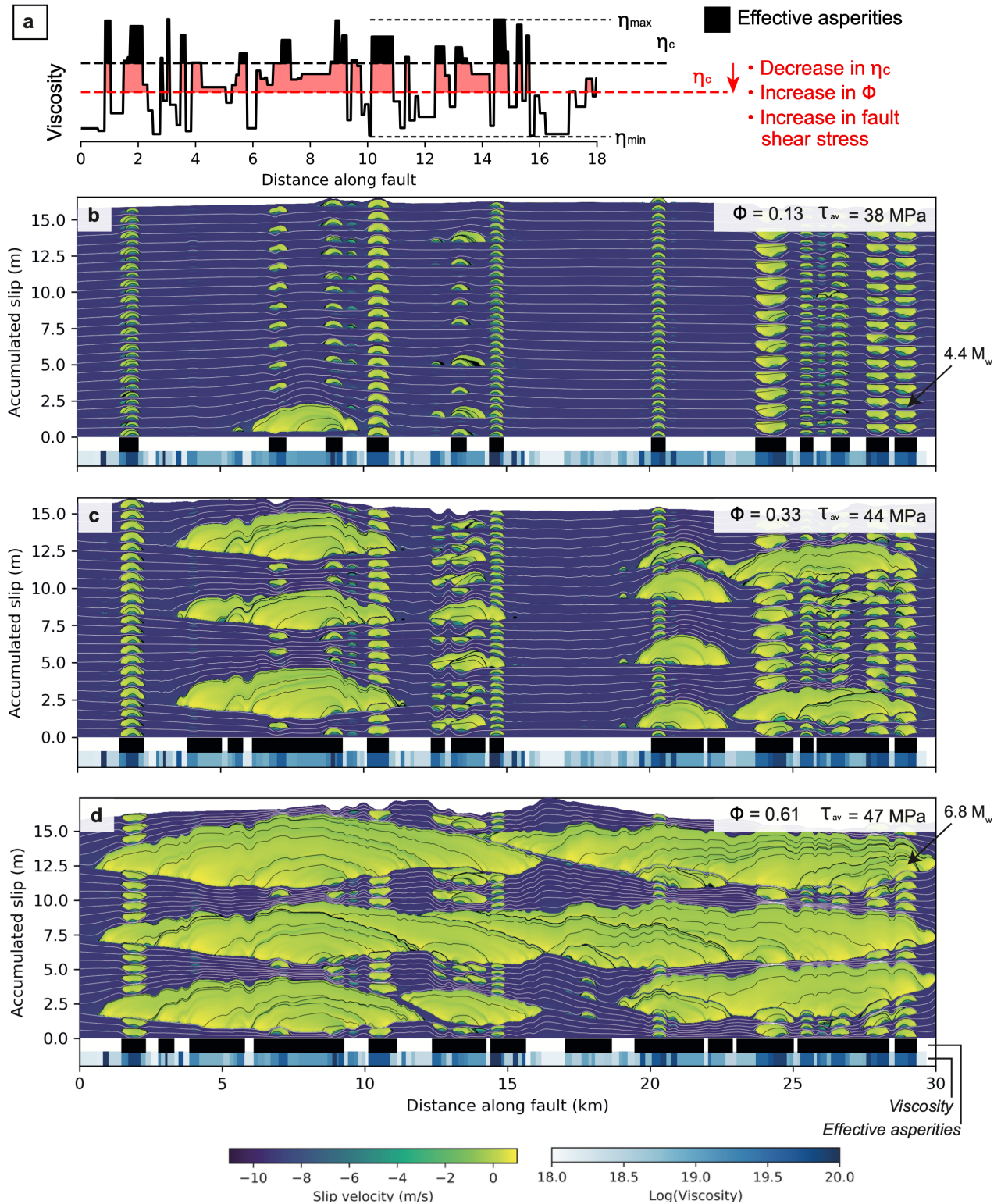
222 earthquakes with $M_w < 6.9$ occur, propagating through regions undergoing inter-seismic creep
223 (interpreted as barriers) ≤ 1 km wide (Figure 1d). Large events occur less frequently than small
224 events, and with greater displacement, as occurs in natural scaling relationships. The largest
225 events in the reference model-set occur when $\phi = 1$ ($W=10$ m) and have $M_w < 7.4$, reaching the
226 limit at which ruptures are restricted by fault length.

227

228

229

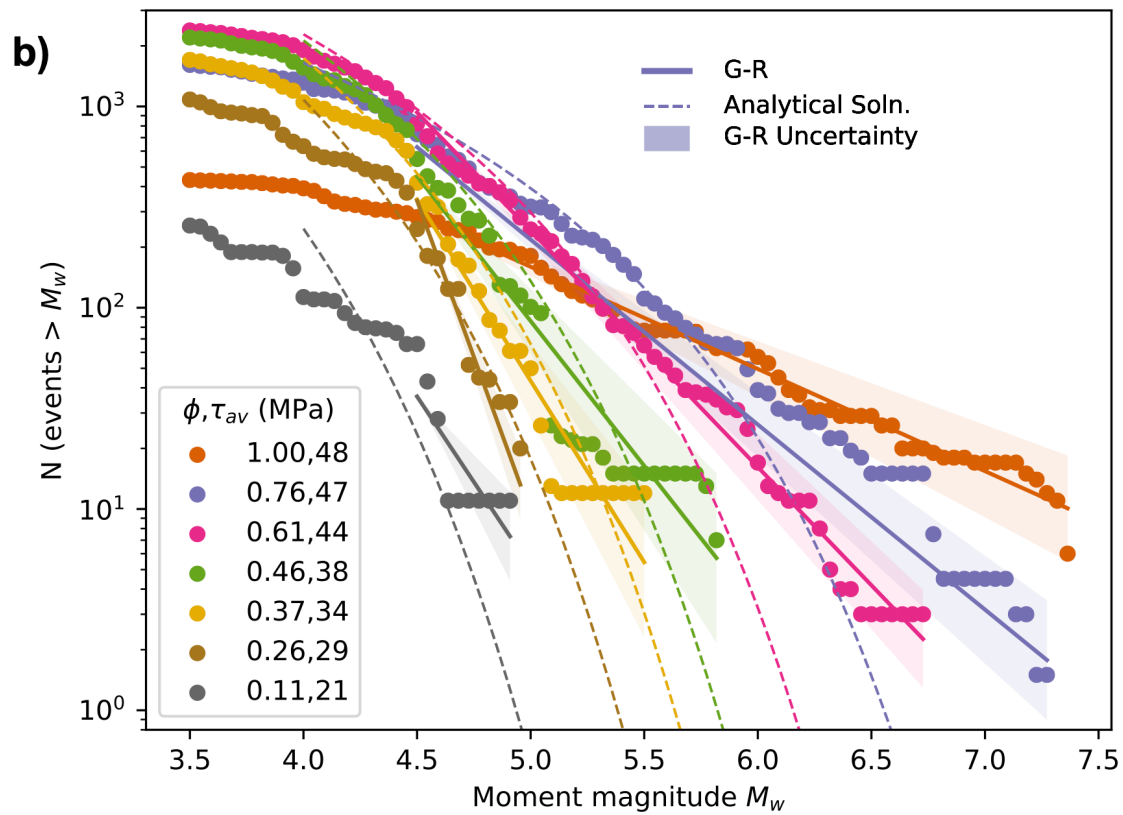
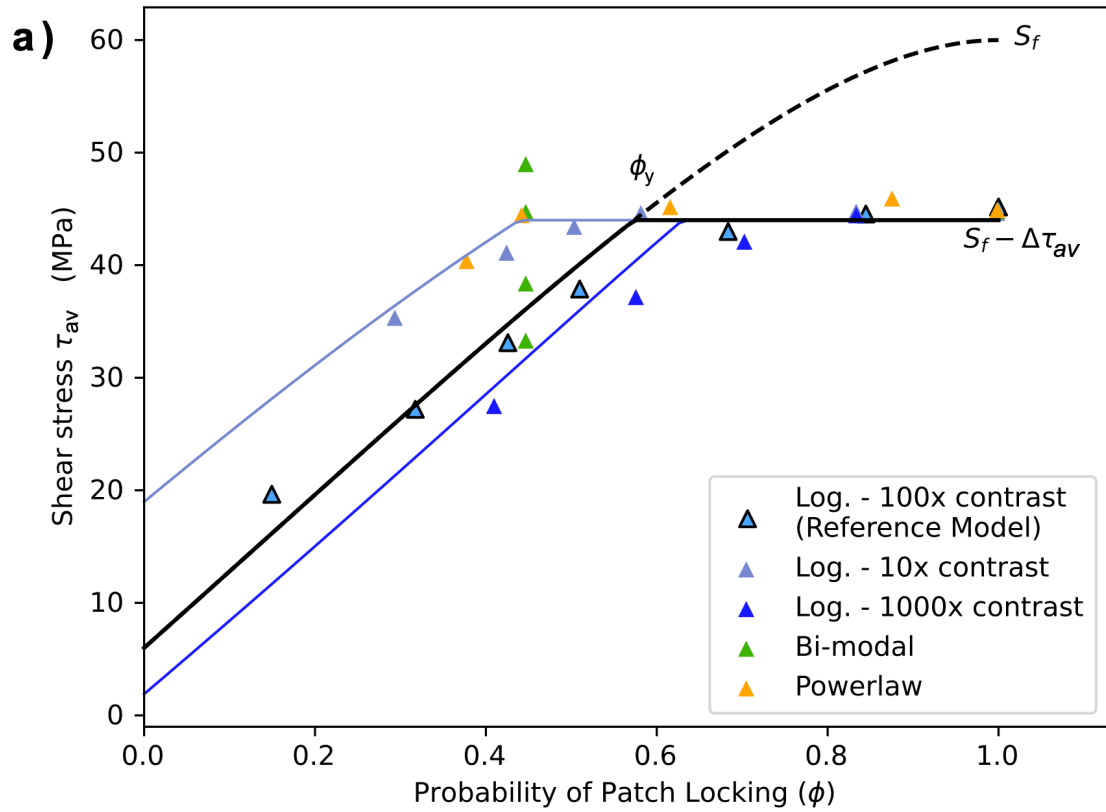
230



231
 232 **Figure 1.** (a) Effective asperities occur where $\eta > \eta_c$ (shaded regions). (b-d) Modelled
 233 seismic (yellow) slip and creep (purple) accumulated over 500 years for reference
 234 models with various ϕ . White curves are separated by inter-seismic intervals of
 235 20 years and black curves by seismic intervals of 2 seconds. Below each plot, the

236
237
238

distributions of viscosity (identical between models) and effective asperities are shown.



240 **Figure 2.** Variation of average shear stress (a) and magnitude statistics (b) between models with
 241 different patch locking probability ϕ . a) Equation 6 is shown for the reference model-set (black
 242 line), with (solid) and without (dashed) capping at a stress $S_f - \Delta\tau$. Lower and higher viscosity
 243 contrasts are also shown by light and dark blue lines respectively. b) The G-R fit (solid lines) and
 244 analytical solution (equation 8) are shown (dashed lines).

245
246

247 3.1 Magnitude recurrence distribution and b-value

248 The recurrence times of seismic events are generally approximated by the G-R law (Figure 2b).
 249 This power-law is fit to the numerical data using a linear regression. Uncertainty is estimated by
 250 measuring the b-value for random subsets (1/3) of the data and taking the standard deviation. The
 251 minimum cut-off magnitude M_c for the G-R fit appears to be ~ 4.5 , corresponding to a length-
 252 scale of 904 m, larger than the average patch length.

253

254 The b-value increases with decreasing ϕ and τ_{max} , reflecting the decreased likelihood of large
 255 events with decreasing stress. The exact b-value is ambiguous for $\phi \sim 0.1$, due to a small M_w
 256 range. Many b-values are within the range of b-values compiled by Nishikawa and Ide (2014) for
 257 subduction zones and all are within the wide range reported in the literature for all settings (El-
 258 Isa & Eaton, 2014). The maximum M_w increases approximately linearly with increasing ϕ , up to
 259 the occurrence of fault-spanning ruptures at $M_w \sim 7.5$ (see also Figure S3).

260

261 To understand the cause of this G-R law, we derive the magnitude recurrence distribution for the
 262 analytical asperity model (Text S3.1-3.4). The expected number of asperities having length L
 263 (assumed to be an integer multiple of w) or larger is:

264

$$E(W \geq L) = \frac{L_f(1 - \phi)\phi^{\frac{L}{w}}}{w} \quad (7)$$

265

266 L_f is the total fault length and this prediction agrees with the numerical data (Figure S7). If each
 267 effective asperity ruptures repeatedly with stress drop $\Delta\tau$, the expected number of events with
 268 length larger than L is:

269

$$E(N \geq N_L) = \frac{(1 - \phi)^2 \gamma \chi_a(\phi) L_f}{w^2} \sum_{n=L/w}^{\infty} \frac{\phi^n}{n} \quad (8)$$

270

271 for $\gamma = tv_p G / (c_s \Delta\tau)$, geometric constant c_s , sampling duration t , shear modulus G and asperity
 272 seismic coupling χ_a . The infinite sum converges because $\phi < 1$, so large ruptures are
 273 increasingly improbable. Event length is converted to M_w , as $L \propto 10^{0.5M_w}$ for constant $\Delta\tau$,
 274 giving the magnitude-recurrence relationship (dashed lines, Figure 2b). Equation 8 is not a
 275 power-law, instead tapering off at high M_w . It has a similar slope to the data and is a good
 276 approximation, but underestimates the number of large magnitude events when $\phi \geq 0.5$, likely
 277 because ruptures propagate between the effective asperities at high ϕ in the numerical models.

278

279 We find an equivalent b-value, by calculating the tangent of equation 8, evaluated at a length-
 280 scale L (ideally slightly higher than the length-scale for M_c), giving:

$$b \equiv -\frac{d \log_{10} E}{d M_w} = \frac{L}{2w} \left(\frac{\sum_{k=0}^{\infty} \frac{\phi^k}{(k + L/w)^2}}{\sum_{k=0}^{\infty} \frac{\phi^k}{k + L/w}} - \ln \phi \right) \quad (9)$$

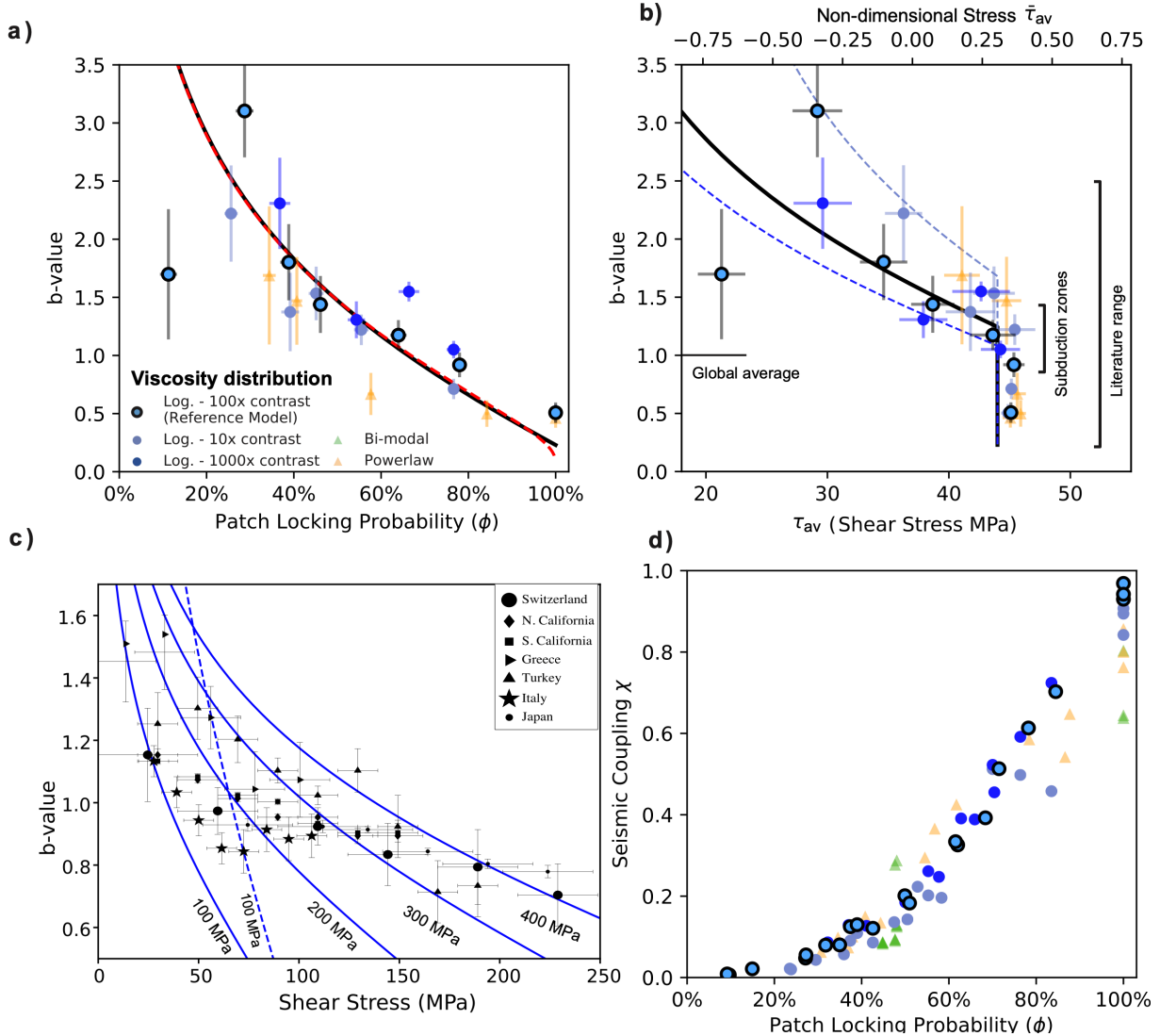
281
 282 This expression is well approximated for $\phi < 0.95$ and $L/w \sim 1$ by:
 283

$$b = \frac{1}{2} - 0.27\phi^2 - \frac{L}{2w} \ln(\phi) \quad (10)$$

284
 285 This b-value only depends on ϕ and L/w . Equation 8 is tangent to the G-R law at $M_w = 5$ for
 286 the numerical models (Figure 2b), corresponding to $L = 1.6$ km, (compared to $w = 550$ m),
 287 giving $L/w = 3$. In this case, the b-value range of 2.5 to 0.3 in nature (El-Isa & Eaton, 2014)
 288 corresponds to $\phi = 0.26$ to 0.97.

289
 290 Equation 10 reproduces the decrease of b-value with increasing ϕ , and agrees well with the
 291 numerical models (Figure 3a). The exact and approximate solutions are mostly indistinguishable.
 292 The b-value estimate is converted to a function of τ_{av} using equation 6. The stress cut-off at $S_f -$
 293 $\Delta\tau_{av}$ explains the sharp decrease of b-value at $\tau_{av} = 43$ MPa ($\bar{\tau}_0 = 0.26$).

294
 295



296
 297 **Figure 3.** a-b) b-value of the numerical models as a function of ϕ (a) and τ_{av} (b). Marker styles
 298 depict the reference model-set (outlined) and alternative viscosity distributions (see legend). The
 299 uncertainty in b-value fit and variation in τ_{av} within each set of random models are shown by
 300 vertical and horizontal bars. The bi-modal distribution model-set does not follow the G-R
 301 distribution and is omitted. a) The exact (red dashed line) and approximate (solid line) analytical
 302 predictions, equations 9 and 10 are shown. b) Equation 10 is shown as a function of stress (solid
 303 line), with light and dark blue dashed lines for smaller and larger viscosity contrasts. c) Natural
 304 b-value estimates (modified from Scholz, 2015) are compared to equation 10 (black line),
 305 assuming $L/w = 1$ and $\tau = m\phi$, where various values of m are labelled in MPa. A case $L/w =$
 306 3 is also shown (dashed line). d) Seismic coupling for all models (marker styles following a).

307

308

309 3.2 Viscosity distribution sensitivity

310

311 We tested the sensitivity of our results to the imposed viscosity probability distribution, using
 312 additional model-sets (symbols in Figure 3a,b,d) with smaller or larger viscosity contrasts, or

313 following power-law or bi-modal (either high or low viscosity) distributions (Text S2; Figure
314 S4). The characteristics of these various models collapse onto similar curves when framed in
315 terms of ϕ , as predicted by the analytical model. All model-sets approximately reproduce the G-
316 R law, except the bi-modal distribution, which is also bi-modal in M_w . Variation of statistics
317 between model-sets arises when instead plotted in terms of shear stress, as also predicted by
318 equation 6.

319 **4 Discussion**

320 Our models analyze the underlying mechanism responsible for the variation of b-value with
321 stress, observed experimentally and in nature. A fault with significant strength variation must be
322 loaded to a relatively high stress for an earthquake to grow to a large magnitude, which has been
323 interpreted to imply that relatively permanent fault properties, such as roughness, control both
324 rupture characteristics and fault stress (Fang & Dunham, 2013). Loading stress depends on
325 tectonic setting and can therefore contrast between faults. Dublanche (2020) explored the
326 influence of stress, varied by changing effective normal stress, on b-value in a rate-and-state
327 earthquake cycle model, but found that this simultaneously affects the nucleation length and
328 leads instead to an increase in b-value with increasing shear stress. We have modelled
329 earthquake cycles on a fault-zone that can be loaded at arbitrary regional shear stresses, by
330 incorporating viscous creep that limits the peak loading stress. Using this method, we can
331 successfully reproduce the relationship between b-value and shear stress, without invoking
332 variations in frictional properties.

333
334 The distribution of asperities and creeping regions on subduction megathrusts has been
335 associated with geometrical and rheological heterogeneity at length scales of 100 m to 1 km
336 (Kirkpatrick et al., 2020), which correspond to our modelled patches. Large earthquakes span
337 distances of 10-100 km and variation in seismogenic behavior has been linked to geometric
338 heterogeneity at such large wavelengths (van Rijnsingen et al., 2018). Alternatively, large
339 earthquakes may be hosted on many small asperities which rupture collectively at high stress
340 (Tormann et al., 2014), corresponding to our modelled effective asperities. In this case, the
341 distribution of earthquake sizes and nucleation sites depends on a combination of inherited
342 properties at small scales and tectonic stress at larger scales. There is subsequently uncertainty in
343 using asperity geometry to constrain the maximum M_w , as they may change effective size or link
344 together with changing stress. The approximate reproduction of the G-R law with our analytical
345 model with uniform patch lengths also indicates that the G-R law does not necessarily reflect
346 power-law distributions of fault properties, but could be a statistical effect dependent on stress.

347
348 We propose that regional shear stress is linked locally to the probability ϕ that a fault segment is
349 locked, which controls variations in earthquake statistics. Similar probabilistic dependence on
350 stress has been proposed to explain b-value variation (Huang & Turcotte, 1988; Scholz, 1968),
351 which we expand on by demonstrating its validity for an earthquake cycle model and with the
352 derivation of a statistical model. In our numerical models ϕ is related to viscous creep, but the
353 ability of our simplified viscosity-independent analytic model to reproduce similar statistics
354 demonstrates that the link between earthquake statistics, ϕ and stress may be more general,
355 explaining its occurrence in experimental data (Scholz, 1968) and nature (discussed next).

356

357 In Figure 3c we compare the derived b-value relationship to the natural data of Scholz (2015),
 358 who combined estimated tectonic stresses with b-value data from Spada et al. (2013). We apply a
 359 factor of 0.5 to their differential stress to convert it to invariant shear stress. The ~100 MPa
 360 stresses shown are higher than the ~10 MPa stress scale used in our models, maybe reflecting
 361 intra-plate stress compared to the lower stress on plate interfaces (Duarte et al., 2015). Our
 362 models only depend on the stress relative to frictional strength and can be rescaled. We assume
 363 that $\tau = m\phi$ (where m is an arbitrary constant), motivated by the linear relationship in our
 364 models (Figure 2a), though neglect the stress cut-off because there is no sharp b-value decrease
 365 at high stress in the data. We also assume $L = w$. Despite the simplifications of our asperity
 366 model, the natural decrease in b-value with increasing stress approximately follows the predicted
 367 logarithmic trend. An alternative case with $L > W$ overestimates the b-value variability with
 368 stress. Most of the data points are in the range $0.8 < b < 1.2$, for which the asperity model
 369 predicts that the probability of fault segments being inter-seismically locked or close to failure
 370 ranges from 25% to 55%, depending on stress. This is in contrast to the view that the crust is
 371 uniformly critically stressed (Townend & Zoback, 2000). Spatial variability in criticality,
 372 potentially corresponding to ϕ , was mapped by Langenbruch et al. (2018), who found that
 373 induced seismicity was more easily triggered in particular regions in the intra-plate USA.

374
 375 ϕ may be inferred from estimates of seismic coupling χ (Figure 3d). We calculate χ as the ratio
 376 of the total accumulated seismic slip to the total loading displacement in the numerical models,
 377 which is equivalent to both seismic and inter-seismic coupling. χ is relatively insensitive to the
 378 choice of viscosity distribution and increases monotonically with ϕ , though following a slightly
 379 non-linear relationship (detailed in Text S3.3).

380
 381 Our models relate b-value and stress, providing future opportunities to integrate tectonic stress
 382 data into probabilistic seismic models. While the maximum M_w depends on stress in our models,
 383 it is underestimated by the asperity model, likely depending on more complex rupture dynamics.
 384 Intra-plate stress has plausible variation sufficient to cover a wider range of seismogenic
 385 behavior (Figure 3c). In subduction megathrusts, under-stressing may occur through the
 386 occurrence of pressure solution creep, which is ubiquitous in exhumed megathrusts (e.g.
 387 Fagereng & Sibson, 2010; Kirkpatrick et al., 2021). Geodynamic estimates indicate a ~20%
 388 variation in plate interface shear stress between subduction regimes (Beall et al., 2021;
 389 Dielforder et al., 2020), which is sufficient to drive significant contrasts in seismicity in our
 390 numerical models. The inferred change in ϕ may then provide a mechanism to explain proposed
 391 variations of b-value with subduction stresses (Nishikawa & Ide, 2014; Scholz & Campos,
 392 2012). As inter-seismic coupling is often well constrained in subduction zones from geodetic
 393 data, the link between ϕ and χ could also be used to constrain ϕ and test our model predictions
 394 as more geophysical observations become available.

395 **5 Conclusions**

396 We use numerical models to demonstrate that a visco-frictional fault with a heterogeneous
 397 distribution of viscously creeping and frictionally locked patches can host earthquakes that
 398 follow the Gutenberg-Richter law. The modelling shows that the decreasing relative contribution
 399 of creep at higher driving stresses can explain the empirical link between b-value and stress.
 400 Analytical models indicate that this relationship can be interpreted more generally in terms of the
 401 probability that fault areas of various sizes are critically stressed. These first model applications

402 highlight the potential to apply earthquake cycle models that incorporate stress-dependent inter-
 403 seismic locking in understanding regional contrasts in seismogenic behavior and earthquake
 404 statistics.

405 **Acknowledgments**

406 Analysis and plotting used the NumPy (Harris et al., 2020) and Matplotlib (Hunter, 2007) Python
 407 libraries. We acknowledge the following funding: European Union's Horizon 2020 research and
 408 innovation program, starting Grant Agreement 715836 MICA (AB, ÅF), support from Monash
 409 University (AB, FAC), French government supported UCAJEDI Investments in the Future
 410 project managed by the National Research Agency (ANR) grant ANR-15-IDEX-01 (MPAvdE)
 411 and 3IA Côte d'Azur Investments in the Future project grant ANR-19-P3IA-0002 (MPAvdE).
 412 We thank Baoning Wu for their constructive review.
 413

414 **Open Research**

415 The models described are available in an online repository at
 416 <https://doi.org/10.5281/zenodo.6153898>.
 417
 418

419 **References**

- 420 Abercrombie, R. E. (1995). Earthquake source scaling relationships from -1 to 5 ML using seismograms recorded at
 421 2.5-km depth. *Journal of Geophysical Research: Solid Earth*, *100*(B12), 24015-24036.
 422 <https://doi.org/10.1029/95JB02397>
- 423 Ampuero, J. P., Ripperger, J., & Mai, P. M. (2006). Properties of dynamic earthquake ruptures with heterogeneous
 424 stress drop. In *Geophysical Monograph Series*.
- 425 Avouac, J.-P. (2015). From Geodetic Imaging of Seismic and Aseismic Fault Slip to Dynamic Modeling of the
 426 Seismic Cycle. *Annual Review of Earth and Planetary Sciences*, *43*(1), 233-271.
 427 <http://www.annualreviews.org/doi/10.1146/annurev-earth-060614-105302>
- 428 Beall, A., Fagereng, Å., Huw Davies, J., Garel, F., & Rhodri Davies, D. (2021). Influence of Subduction Zone
 429 Dynamics on Interface Shear Stress and Potential Relationship with Seismogenic Behavior. *Geochemistry,*
 430 *Geophysics, Geosystems*.
- 431 Bilek, S. L., & Lay, T. (2018). Subduction zone megathrust earthquakes. *Geosphere*.
- 432 Bos, B., & Spiers, C. J. (2002). Frictional-viscous flow of phyllosilicate-bearing fault rock: Microphysical model
 433 and implications for crustal strength profiles. *Journal of Geophysical Research: Solid Earth*, *107*(B2), ECV
 434 1-13. <https://doi.org/10.1029/2001JB000301>
- 435 Cattania, C. (2019). Complex Earthquake Sequences On Simple Faults. *Geophysical Research Letters*.
- 436 Dielforder, A., Hetzel, R., & Oncken, O. (2020). Megathrust shear force controls mountain height at convergent
 437 plate margins. *Nature*.
- 438 Duarte, J. C., Schellart, W. P., & Cruden, A. R. (2015). How weak is the subduction zone interface? *Geophysical*
 439 *Research Letters*.
- 440 Dublanchet, P. (2020). Stress-Dependent b Value Variations in a Heterogeneous Rate-and-State Fault Model.
 441 *Geophysical Research Letters*.
- 442 Dublanchet, P., Bernard, P., & Favreau, P. (2013). Interactions and triggering in a 3-D rate-and-state asperity model.
 443 *Journal of Geophysical Research: Solid Earth*, *118*(5), 2225-2245. <https://doi.org/10.1002/jgrb.50187>
- 444 El-Isa, Z. H., & Eaton, D. W. (2014). Spatiotemporal variations in the b-value of earthquake magnitude-frequency
 445 distributions: Classification and causes. *Tectonophysics*, *615-616*, 1-11.
 446 <http://dx.doi.org/10.1016/j.tecto.2013.12.001>
- 447 Fagereng, Å., & Sibson, R. H. (2010). Mélange rheology and seismic style. *Geology*, *38*(8), 751-754.
- 448 Fang, Z., & Dunham, E. M. (2013). Additional shear resistance from fault roughness and stress levels on
 449 geometrically complex faults. *Journal of Geophysical Research: Solid Earth*.

- 450 Galis, M., Pelties, C., Kristek, J., Moczo, P., Ampuero, J. P., & Mai, P. M. (2015). On the initiation of sustained
451 slip-weakening ruptures by localized stresses. *Geophysical Journal International*, 200(2), 888-907.
452 <https://academic.oup.com/gji/article-lookup/doi/10.1093/gji/ggu436>
- 453 Gerstenberger, M. C., Marzocchi, W., Allen, T., Pagani, M., Adams, J., Danciu, L., et al. (2020). Probabilistic
454 Seismic Hazard Analysis at Regional and National Scales: State of the Art and Future Challenges. *Reviews*
455 *of Geophysics*, 58(2), 1-49.
- 456 Gratier, J. P., Thouvenot, F., Jenatton, L., Tourette, A., Doan, M. L., & Renard, F. (2013). Geological control of the
457 partitioning between seismic and aseismic sliding behaviours in active faults: Evidence from the Western
458 Alps, France. *Tectonophysics*, 600, 226-242. <http://dx.doi.org/10.1016/j.tecto.2013.02.013>
- 459 Harris, C. R., Millman, K. J., van der Walt, S. J., Gommers, R., Virtanen, P., Cournapeau, D., et al. (2020). Array
460 programming with NumPy. *Nature*, 585(7825), 357-362. <https://doi.org/10.1038/s41586-020-2649-2>
- 461 Huang, J., & Turcotte, D. L. (1988). Fractal distributions of stress and strength and variations of b-value. *Earth and*
462 *Planetary Science Letters*, 91(1), 223-230.
463 <https://www.sciencedirect.com/science/article/pii/0012821X88901641>
- 464 Hunter, J. D. (2007). Matplotlib: A 2D graphics environment. *Computing in Science & Engineering*, 9(3), 90-95.
- 465 Kanamori, H., & Anderson, D. L. (1975). Theoretical basis of some empirical relations in seismology. *Bulletin of*
466 *the Seismological Society of America*, 65(5), 1073-1095.
- 467 King, G. (1983). The accommodation of large strains in the upper lithosphere of the earth and other solids by self-
468 similar fault systems: the geometrical origin of b-Value. *Pure and Applied Geophysics*, 121(5), 761-815.
469 <https://doi.org/10.1007/BF02590182>
- 470 Kirkpatrick, J. D., Edwards, J. H., Verdecchia, A., Kluesner, J. W., Harrington, R. M., & Silver, E. A. (2020).
471 Subduction megathrust heterogeneity characterized from 3D seismic data. *Nature Geoscience*, 13(5), 369-
472 374. <https://doi.org/10.1038/s41561-020-0562-9>
- 473 Kirkpatrick, J. D., Fagereng, Å., & Shelly, D. R. (2021). Geological constraints on the mechanisms of slow
474 earthquakes. *Nature Reviews Earth & Environment*, 2(4), 285-301.
- 475 Lambert, V., Lapusta, N., & Faulkner, D. (2021). Scale Dependence of Earthquake Rupture Prestress in Models
476 With Enhanced Weakening: Implications for Event Statistics and Inferences of Fault Stress. *Journal of*
477 *Geophysical Research: Solid Earth*, 126(10), e2021JB021886.
478 <https://agupubs.onlinelibrary.wiley.com/doi/abs/10.1029/2021JB021886>
- 479 Langenbruch, C., Weingarten, M., & Zoback, M. D. (2018). Physics-based forecasting of man-made earthquake
480 hazards in Oklahoma and Kansas. *Nature Communications*, 9(1), 3946. <https://doi.org/10.1038/s41467-018-06167-4>
- 481
- 482 Luo, Y., Ampuero, J. P., Galvez, P., Ende, M. v. d., & Idini, B. (2017). QDYN: a Quasi-DYNAMIC earthquake
483 simulator (v1.1).
- 484 Mogi, K. (1967). Earthquakes and fractures. *Tectonophysics*, 5(1), 35-55.
485 <https://www.sciencedirect.com/science/article/pii/0040195167900431>
- 486 Nishikawa, T., & Ide, S. (2014). Earthquake size distribution in subduction zones linked to slab buoyancy. *Nature*
487 *Geoscience*.
- 488 Nuannin, P., Kulhanek, O., & Persson, L. (2005). Spatial and temporal b value anomalies preceding the devastating
489 off coast of NW Sumatra earthquake of December 26, 2004. *Geophysical Research Letters*, 32(11).
490 <https://doi.org/10.1029/2005GL022679>
- 491 Rice, J. R. (1993). Spatio-temporal complexity of slip on a fault. *Journal of Geophysical Research*, 98(B6), 9885-
492 9885. <http://doi.wiley.com/10.1029/93JB00191>
- 493 Rice, J. R., & Ben-Zion, Y. (1996). Slip complexity in earthquake fault models. *Proceedings of the National*
494 *Academy of Sciences of the United States of America*.
- 495 Ripperger, J., Ampuero, J. P., Mai, P. M., & Giardini, D. (2007). Earthquake source characteristics from dynamic
496 rupture with constrained stochastic fault stress. *Journal of Geophysical Research: Solid Earth*.
- 497 Rubin, A. M., & Ampuero, J. P. (2005). Earthquake nucleation on (aging) rate and state faults. *Journal of*
498 *Geophysical Research: Solid Earth*.
- 499 Rutter, E. (1976). A discussion on natural strain and geological structure-the kinetics of rock deformation by
500 pressure solution. *Philosophical Transactions of the Royal Society of London. Series A, Mathematical and*
501 *Physical Sciences*, 283(1312), 203-219.
- 502 Scholz, C. H. (1968). The frequency-magnitude relation of microfracturing in rock and its relation to earthquakes.
503 *Bulletin of the Seismological Society of America*.
- 504 Scholz, C. H. (2015). On the stress dependence of the earthquake b value. *Geophysical Research Letters*.

- 505 Scholz, C. H., & Campos, J. (2012). The seismic coupling of subduction zones revisited. *Journal of Geophysical*
506 *Research: Solid Earth*, 117(5).
- 507 Schorlemmer, D., Wiemer, S., & Wyss, M. (2005). Variations in earthquake-size distribution across different stress
508 regimes. *Nature*.
- 509 Spada, M., Tormann, T., Wiemer, S., & Enescu, B. (2013). Generic dependence of the frequency-size distribution of
510 earthquakes on depth and its relation to the strength profile of the crust. *Geophysical Research Letters*.
- 511 Tormann, T., Wiemer, S., & Mignan, A. (2014). Systematic survey of high-resolution b value imaging along
512 Californian faults: Inference on asperities. *Journal of Geophysical Research: Solid Earth*, 119(3), 2029-
513 2054.
- 514 Townend, J., & Zoback, M. D. (2000). How faulting keeps the crust strong. *Geology*, 28(5), 399-402.
515 [https://doi.org/10.1130/0091-7613\(2000\)28<399:HFKTCS>2.0.CO;2](https://doi.org/10.1130/0091-7613(2000)28<399:HFKTCS>2.0.CO;2)
- 516 van den Ende, M. P. A., Chen, J., Niemeijer, A. R., & Ampuero, J. P. (2020). Rheological Transitions Facilitate
517 Fault-Spanning Ruptures on Seismically Active and Creeping Faults. *Journal of Geophysical Research:*
518 *Solid Earth*, 125(8), 1-27.
- 519 van Rijsingen, E., Lallemand, S., Peyret, M., Arcay, D., Heuret, A., Funiciello, F., & Corbi, F. (2018). How
520 Subduction Interface Roughness Influences the Occurrence of Large Interplate Earthquakes. *Geochemistry,*
521 *Geophysics, Geosystems*.
- 522